

Cite this: *RSC Adv.*, 2017, 7, 56447

Investigation of the interactions in CeO₂–Fe₂O₃ binary metal oxides supported on ZSM-5 for NO removal by CO in the presence of O₂, SO₂ and steam

Yuting Bai, Wenyuan Wu^{ID}* and Xue Bian

ZSM-5 series catalysts with different metal contents were prepared for NO removal by CO in the presence of O₂, SO₂ and steam via an impregnation method. The flash catalysts and used catalysts were characterized via XRD, BET, XPS, NH₃-TPD, CO-TPR and *in situ* DRIFTS and their activities were tested in a fixed-bed reactor. The 10Ce–10Fe catalyst exhibited stable NO conversion of over 90% within the temperature range from 320 °C to 650 °C, and it has superior resistance to O₂, SO₂ and steam. The ZSM-5 structure was retained after loading Fe and Ce, and diffraction peaks of Fe₂O₃ and CeO₂ were observed in the XRD spectra with an increase in the metal content. The specific surface area and pore volume of Ce–Fe/ZSM-5 decreased, and its average pore diameter increased. The Ce–Fe/ZSM-5 catalysts possess chemisorbed oxygen and lattice oxygen, and their various cations (Fe³⁺/Fe²⁺ and Ce⁴⁺/Ce³⁺) promote the production of oxygen vacancies, which are beneficial for the activation of N–O. The strong acid sites and some medium-strong acid sites are involved in the catalytic reaction as the active sites for Ce–Fe/ZSM-5 in NH₃-TPD. The interaction between Fe₂O₃ and CeO₂ (Ce³⁺ + Fe³⁺ ↔ Ce⁴⁺ + Fe²⁺) in the Ce–Fe/ZSM-5 catalyst improves its catalytic performance, reducing property, resistance to O₂, SO₂ and steam, and service life.

Received 29th September 2017
Accepted 4th December 2017

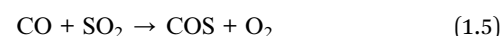
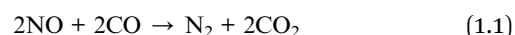
DOI: 10.1039/c7ra10773k

rsc.li/rsc-advances

1. Introduction

Nitrogen oxides (NO_x) are one of the predominant severe pollutants in the atmosphere, which cause acid rain, ozone depletion, photochemical smog, greenhouse effects, *etc.*¹ Currently, selective catalytic reduction (SCR) of NO_x with NH₃ in 2–6 vol% O₂ is an efficient technology for the abatement of NO_x from stationary sources, such as power plants.^{2,3} The narrow temperature window (300–400 °C), high toxicity of vanadium species (V₂O₅), SO₂ oxidation to SO₃, and formation of N₂O at high temperatures are disadvantages for the widely used commercial catalyst, V₂O₅–WO₃ (MoO₃)/TiO₂.^{4,5} Therefore, low-temperature SCR with non-polluting catalysts has attracted increasing attention. Its reactor is generally located downstream of the electrostatic precipitator and desulfurization device to avoid catalyst deactivation caused by the high concentration of ash.⁶ However, through extensive research on low-temperature SCR catalysts in recent years, it was found that the operating temperature window (150–300 °C) for low-temperature SCR catalysts^{7,8} is slightly higher than the flue gas temperature (50–100 °C) from the desulfurizer, and ammonium sulfate, which is formed in the presence of a small

amount of SO₂ (about 50 ppm), results in catalyst deactivation.⁴ Due to the ability of reducing SO₂ and its wide existence in flue gas, CO is a promising reductant for stationary sources, particularly coal-fired power plants with a high CO content in their exhaust gas. CO was used in this study as a reducing agent to remove NO similar to automobile exhaust purification.^{9,10} Compared with mobile source systems, CO oxidation by O₂ and the formation of hypertoxic COS by-products are the difficulties associated with this investigation and application. The main related reactions are represented by eqn (1.1)–(1.5):



Various catalysts for NO reduction by CO have been investigated, such as CuO–CoO/γ-Al₂O₃,¹¹ CuO/CeO₂–TiO₂,¹² MnO_x–CuO/Ce_{0.67}Zr_{0.23}O₂ (ref. 13) and CuO–CeO₂,¹⁴ but their resistance to O₂ and SO₂ is rarely considered. Pereira *et al.*¹⁵ researched the stability of CuO/TiO₂ and FeO/TiO₂ catalysts

School of Metallurgy, Northeastern University, Shen Yang, 110819, China. E-mail: wuwuy@smm.neu.edu.cn

during NO reduction by CO in the presence of O₂ and SO₂. The results showed that the presence of O₂ leads to the direct oxidation of CO to CO₂ according to eqn (1.3), and the conversion of NO decreases drastically when SO₂ is added into the feed stream due to the formation of sulfates on the titania surface, which block the active sites. Li *et al.*¹⁶ researched an Fe-based catalyst for the reduction of NO by CO under FCC regeneration conditions, and suggested that Fe-based catalysts enhance the reduction of NO by CO at a lower temperature and the reaction rate decreases with an increase in O₂ concentration.

Zeolite ZSM-5, which has a porous structure and rich acid sites, is considered to be a perfect carrier for extensive use in many types of catalytic reactions, such as catalytic cracking and catalytic dehydration.^{17,18} Cu/ZSM-5 and Fe/ZSM-5 are usually used for NH₃-SCR, and it has been shown that the characteristics of Fe/ZSM-5 are conducive to NO reduction. The NO_x conversion over Fe-CuO_x/ZSM-5 catalyst reached 98% within the temperature range of 180 to 360 °C.¹⁹ Li *et al.*²⁰ indicated that Fe₂O₃ is a good adsorbent for both NO and NO₂, while H-ZSM-5 is not a good adsorbent for either NO or NO₂. Fe-ZSM-5 only adsorbs NO₂, which strongly demonstrates the existence of interactions between the Fe_xO_y clusters and the zeolite support. Nevertheless, the use of zeolite ZSM-5 for NO_x removal by CO is unusual. Cheng *et al.*²¹ discovered that NO_x removal over Fe/ZSM-5 catalysts is very stable at 250–400 °C in a simulated rotary reactor with 5% O₂, and a higher CO concentration enhances the reduction efficiencies.

Ce-doped catalysts, including CuO/CeO₂-TiO₂,²² CeWO_x,²³ Ce-Cu/ZSM-5 (ref. 24) and Ce-Mn/ZSM-5,²⁵ have been reported recently because Ce can store and release oxygen *via* the Ce³⁺/Ce⁴⁺ redox cycle. Deng *et al.*²² showed that the strong synergistic effect between Ti³⁺, Ce³⁺ and Cu⁺ in CuO/CeO₂-TiO₂ is beneficial to improve activity due to more oxygen vacancies. Lai *et al.*²⁴ elucidated that the addition of Ce increases the Lewis acid sites on the surface of Cu/ZSM-5 and broadens the operation temperature window. However, studies about Ce and Fe modified ZSM-5 are relatively scarce.

Herein, a series of Fe/ZSM-5 and Ce-Fe/ZSM-5 catalysts with different Fe and Ce contents were prepared *via* impregnation, and their catalytic activity for NO reduction by CO in the presence of O₂ and SO₂ was further evaluated. Then, the samples were characterized *via* XRD, BET, XPS, NH₃-TPD, CO-TPR and *in situ* DRIFTS. The interactions in the CeO₂-Fe₂O₃ binary metal oxides supported on ZSM-5 were thoroughly investigated.

2. Experimental

2.1 Catalyst preparation

ZSM-5 zeolites were synthesized *via* the seeding method in a hydrothermal system using silica sol, sodium aluminate and sodium hydroxide as the main raw materials. The ZSM-5 seed crystals were obtained from Nankai University, silica sol was procured by Guangzhou Suixin Chemical Industry Co., Ltd, and the other reagents were purchased from Sinopharm Chemical Reagent Co., Ltd, which were of analytical grade (AR). The HZSM-5 support was obtained after ion exchange with ammonium nitrate.

The Fe/ZSM-5 samples were prepared by the conventional wet impregnation of HZSM-5 with an aqueous solution containing the required amount of Fe(NO₃)₃·9H₂O. The samples were dried at 110 °C for 10 h and then calcined at 550 °C in air for 4 h. The products were simply denoted as *x*Fe/ZSM-5, where *x* represents the mass percent of Fe in the catalyst. 0Fe/ZSM-5 was pure HZSM-5. *x*Fe/ZSM-5-A represents the used *x*Fe/ZSM-5 catalyst after catalytic reaction for 24 h. Similarly, the Ce-Fe/ZSM-5 catalyst was prepared by the wet impregnation of HZSM-5 with Fe(NO₃)₃·9H₂O and Ce(NO₃)₃·6H₂O, which was denoted as *y*Ce-*x*Fe/ZSM-5, where *x* and *y* represent the mass percent of Fe and Ce in the catalyst, respectively.

2.2 Characterizations

X-ray diffraction (XRD) patterns were recorded on a Dutch X'pert HighScore Plus X-ray diffractometer using Cu K α radiation in the 2 θ range of 5–90° with a step of 2° min⁻¹. The X-ray tube was operated at 40 kV and 40 mA. The quantitative analysis of TFe and FeO was performed *via* a chemical titration method.

Nitrogen adsorption-desorption isotherms were measured at 77 K on a Micrometrics ASAP-2020 adsorption apparatus. Samples were placed under vacuum for 4 h at 400 °C as a pretreatment. Specific surface area was determined using the Brunauer-Emmett-Teller (BET) method. The pore volume and aperture size were calculated using the Barrett-Joyner-Halenda (BJH) formula.

X-ray photoelectron spectroscopy (XPS) was performed on a Thermo Scientific Escalab 250Xi using Al K α as the radiation source at 150 W. The binding energies (BEs) were referenced to the adventitious C 1s at 284.6 eV. This reference gave BE values with an accuracy of ± 0.1 eV.

NH₃ temperature-programmed desorption (NH₃-TPD) was carried out on a PX200 apparatus by Tianjin Pengxiang Technology Ltd. About 100 mg sample was placed in a quartz reactor and pretreated at 500 °C under a flow of N₂ (70 mL min⁻¹) for 1 h. The amount of NH₃ desorbed was detected by a thermal conductivity detector (TCD).

Carbon monoxide temperature-programmed reduction (CO-TPR) was performed on a Micromeritics Autochem 2920 equipped with TCD. Initially, 50 mg sample was pretreated under N₂ flow at 300 °C for 1 h. After cooling to room temperature, the sample was heated to 800 °C (10 °C min⁻¹) under a CO-N₂ mixture (10% CO by volume).

In situ diffuse reflectance infrared Fourier transform spectra (*in situ* DRIFTS) were collected from 400 to 4000 cm⁻¹ at a spectral resolution of 4 cm⁻¹ (number of scans: 32) on a Nicolet IS50 FT-IR spectrometer equipped with a high-sensitive MCT detector. The sample was placed on a high temperature cell and pretreated with N₂ at 300 °C for 1 h. The background of each target temperature was collected during the cooling process; then, the sample was exposed to a controlled stream of CO-Ar (10% vol. CO) or/and NO-Ar (5% vol. NO) at a rate of 10 mL min⁻¹ for 30 min. Desorption/reaction studies were performed by heating the adsorbed species and the spectra were recorded at target temperatures from room temperature to 350 °C at the rate of 10 °C min⁻¹ by subtracting the corresponding background reference.



2.3 Evaluation of catalytic performance

Catalyst activity tests were carried out in a fixed-bed reactor with 5 mL sample (40–60 mesh) between 200 °C and 650 °C. The gas mixture contained 600 ppm NO, 600 ppm CO, and N₂ as diluents with a space velocity of 36 000 h^{−1}. The product was analyzed *via* gas chromatography (GC9310) with TCD and two columns (Porapak Q and Molecular 13X). The 10Fe/ZSM-5 and 10Ce-10Fe/ZSM-5 catalysts were also evaluated in the reduction of NO with CO at 400 °C in the presence of 1000 ppm O₂, 60 ppm or 120 ppm SO₂, and 3% water steam. The conversion (η) of NO was calculated using eqn (2.1).

$$\eta = \frac{([\text{NO}]_{\text{inlet}} - [\text{NO}]_{\text{outlet}})}{[\text{NO}]_{\text{inlet}}} \times 100\% \quad (2.1)$$

3. Results and discussion

3.1 Catalytic activity

NO conversion as a function of reaction temperature between 200 °C and 650 °C on the series of ZSM-5 catalysts with different metal contents is shown in Fig. 1(a), the reaction temperature ($T_{10\%}$, $T_{90\%}$, and $T_{100\%}$) and maximal conversion are listed in Table 1. The 0Fe/ZSM-5 catalyst presented almost no activity in the working temperature window. The 2Fe/ZSM-5 catalyst exhibited significant catalytic activity at the $T_{10\%}$ of 379 °C and the highest conversion of NO reached 89.24%. The $T_{10\%}$ of the 5Fe/ZSM-5 catalyst decreased to 318 °C, and the NO conversion reached 100% at 476 °C. However, with an increase in temperature to 580 °C, the NO conversion declined. The NO conversion curve of 10Fe/ZSM-5 clearly shifted to a low temperature, and $T_{90\%}$ decreased to about 80 °C compared with that of 5Fe/ZSM-5. Besides, the NO conversion remained at 100% up until 650 °C, which broadened the operating temperature window. Briefly, with an increase in Fe content in the catalyst, the NO conversion significantly increased and the catalytic reaction temperature gradually decreased. After adding Ce, the NO conversion curve of the 5Ce-10Fe/ZSM-5 catalyst also shifted to low temperature, and $T_{90\%}$ dropped by nearly 20 °C to 338 °C. The $T_{90\%}$ of the 10Ce-10Fe/ZSM-5 catalyst further decreased to 317 °C, which showed the best performance. However, the

Table 1 The temperatures of 10%, 90%, and 100% NO conversion and maximal conversion for the different catalysts

Catalyst	$T_{10\%}$ (°C)	$T_{90\%}$ (°C)	$T_{100\%}$ (°C)	η_{Max} (%)
0Fe/ZSM-5	—	—	—	5.52
2Fe/ZSM-5	379	—	—	89.24
5Fe/ZSM-5	318	434	476	100.00
10Fe/ZSM-5	277	356	411	100.00
10Ce/ZSM-5	445	578	623	100.00
5Ce-10Fe/ZSM-5	234	338	360	100.00
10Ce-10Fe/ZSM-5	214	317	380	100.00

10Ce/ZSM-5 catalyst exhibited poor activity, and 445 °C was too high for $T_{10\%}$, which shows that the catalytic activity of the Fe species is better than Ce. Above all, these results illustrates that Ce has a promoting effect on the catalytic reaction. The N₂ selectivity curves (Fig. 1(b)) shifted to a low temperature with an increase in the metal contents, which are similar to the NO conversion curves. The N₂ selectivities increased when the reaction temperature increased as a result of the rapid decomposition of absorbed NO on the catalyst surface at high temperature.

The performances of resistance to O₂, SO₂ and steam on the 10Fe/ZSM-5 and 10Ce-10Fe/ZSM-5 catalysts are shown in Fig. 2. The main components of the initial feed stream were 1200 ppm CO and 600 ppm NO. The NO conversion over the 10Fe/ZSM-5 catalyst was 100% at 400 °C. When 60 ppm SO₂ was added, the conversion of NO to N₂ constantly remained 100%. However, the conversion of CO to CO₂ slowly increased due to the redox reaction between CO and SO₂ according to eqn (1.4), and returned to the original value when the SO₂ feed was interrupted. The NO conversion rapidly reduced to 53.8% and CO conversion clearly increased to 87.5% after 1000 ppm O₂ and 60 ppm SO₂ were introduced into the stream. There was a competitive relationship between CO + NO and CO + O₂, and O₂ favored CO oxidation to CO₂. When the O₂ and SO₂ streams were off, the NO conversion recovered to 85.4% but could not reach 100%, indicating that the catalyst was deactivated as a result of some irreversible changes. The NO conversion dropped drastically to 45.8% because the high SO₂ concentration of 120 ppm in the flue gas inhibited the catalyst activity. For

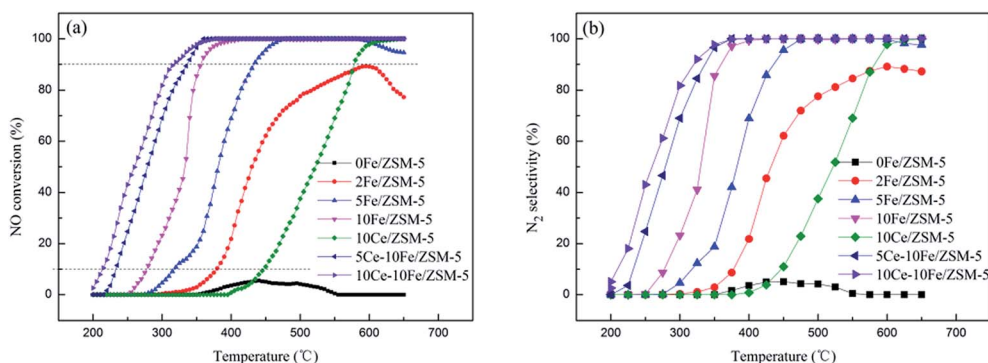


Fig. 1 (a) NO conversion and (b) N₂ selectivity over the ZSM-5 series catalysts with different metal contents.



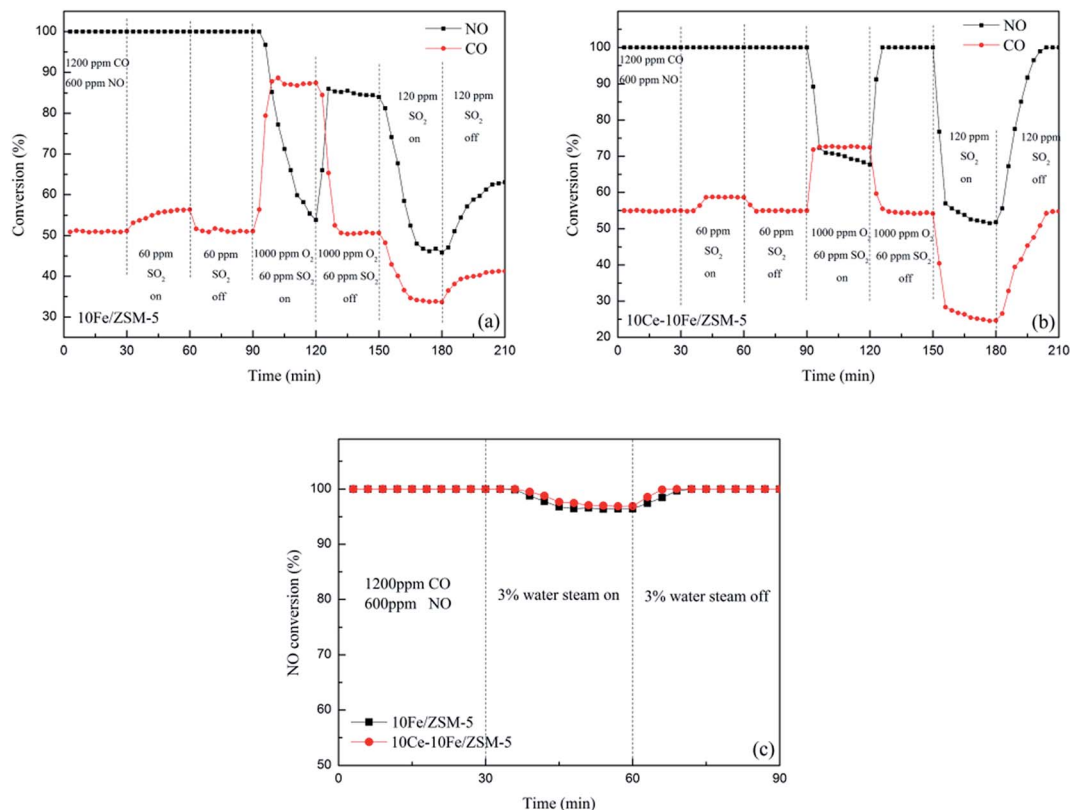


Fig. 2 Conversion of NO to N₂ and CO to CO₂ in the presence of O₂ and SO₂ on (a) 10Fe/ZSM-5 and (b) 10Ce-10Fe/ZSM-5 and (c) NO conversion in the presence of steam at 400 °C.

the 10Ce-10Fe/ZSM-5 catalyst, the resistance curve to O₂ and SO₂ was similar to that for 10Fe/ZSM-5. However, in the presence of 60 ppm SO₂, the CO conversion increased and remained steady. The NO conversion decreased to 67.7% (higher than that for 10Fe/ZSM-5) and the CO conversion increased to 72.5% when 1000 ppm O₂ and 60 ppm SO₂ were added, and the NO conversion recovered to 100% after the O₂ and SO₂ streams were turned off. The NO conversion declined to 51.8% in the presence of 120 ppm SO₂, which exhibits preferable resistance to a high SO₂ concentration. Fig. 2(c) shows that the NO conversions on 10Fe/ZSM-5 and 10Ce-10Fe/ZSM-5 at 400 °C remained

almost unchanged (over 95%) in the presence of steam. In contrast, the 10Ce-10Fe/ZSM-5 catalyst exhibited superior resistance to O₂, SO₂ and steam, and could not be deactivated under the research conditions.

3.2 XRD results

Fig. 3 shows the XRD patterns of the catalysts. All the samples with different contents of active components exhibit the complete typical diffraction peaks of ZSM-5. The used catalysts, 10Fe/ZSM-5-A and 10Ce-10Fe/ZSM-5-A, still retained the

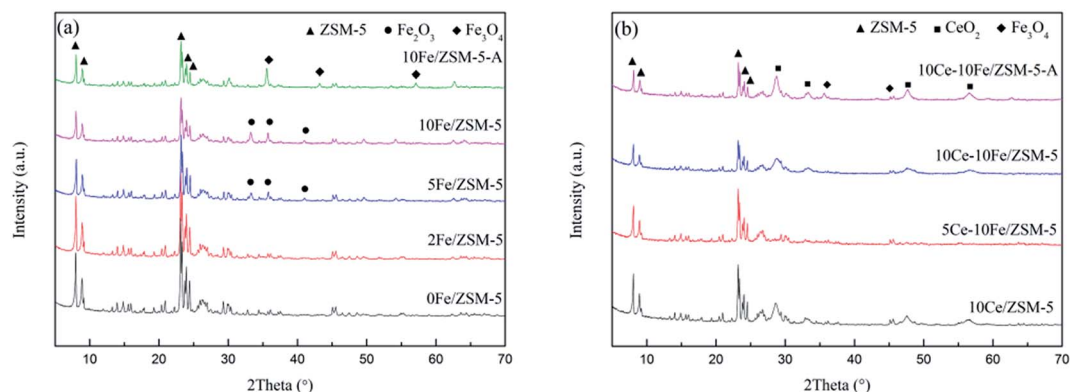


Fig. 3 XRD patterns of the (a) Fe/ZSM-5 catalysts and (b) Ce-Fe/ZSM-5 catalysts.



Table 2 TFe and FeO contents of the ZSM-5 series catalysts

Catalysts	TFe (%)	FeO (%)	Fe ²⁺ (%)	Fe ³⁺ (%)
0Fe/ZSM-5	—	—	—	—
2Fe/ZSM-5	1.96	0.12	0.09	1.87
5Fe/ZSM-5	4.71	0.13	0.10	4.61
10Fe/ZSM-5	9.52	0.11	0.09	9.43
10Fe/ZSM-5-A	10.6	3.26	2.54	8.06
10Ce-10Fe/ZSM-5	9.45	0.12	0.09	9.36
10Ce-10Fe/ZSM-5-A	9.57	0.16	0.12	9.45

structure of ZSM-5. This demonstrates that the frame structure of ZSM-5 as a catalyst carrier did not change during the preparation and reaction process. The quantitative analysis of the different valence states of the Fe_xO_y species through the chemical titration method are shown in Table 2. The low Fe²⁺ content (about 0.09–0.10 wt%) implies that the Fe_xO_y species was primarily Fe₂O₃. As shown in Fig. 3(a), when the Fe content was lower, the diffraction peaks of Fe₂O₃ were hardly observed in the 2Fe/ZSM-5 catalyst, which implies that Fe₂O₃ was highly dispersed on the internal and external surfaces of the carrier. The evident characteristic diffraction peaks of Fe₂O₃ were observed when the Fe content was 5%, and peaks of Fe₂O₃ gradually strengthened with an increase in Fe content. The literature²⁴ shows that metal oxide is amorphous at a low loading content, and under a high loading content, enriched metal oxide on the surface could be crystalline, which has evident characteristic peaks. In the XRD spectra of the used 10Fe/ZSM-5-A catalyst, the typical Fe₂O₃ peaks disappeared, but the characteristic diffraction peaks of Fe₃O₄ appeared, which is in agreement with the increase in Fe²⁺ content to 2.54 wt% in Table 2. This could be due to the reduction of Fe₂O₃ to Fe₃O₄ under the CO atmosphere. It can be seen from Fig. 3(b) that there were no typical diffraction peaks of CeO₂ over 5Ce-10Fe/ZSM-5, and the CeO₂ peaks appeared when the Ce content reached 10%, which is similar to Fig. 3(a). In addition, the characteristic peaks of Ce₂O₃ were not detected due to its instability. The Fe²⁺ content only increased slightly to 0.12 wt% in Table 2, and the Fe₃O₄ peaks in 10Ce-10Fe/ZSM-5-A catalyst were weaker than that in 10Fe/ZSM-5-A, suggesting that Ce inhibits the reduction of Fe₂O₃.

Table 3 Textural properties of the ZSM-5 series catalysts

Catalyst	S _{BET} ^a (m ² g ⁻¹)	V _p ^b (cm ³ g ⁻¹)	D _A ^c (nm)
0Fe/ZSM-5	341.49	0.13	6.25
5Fe/ZSM-5	321.76	0.12	7.18
10Fe/ZSM-5	294.01	0.11	6.95
10Fe/ZSM-5-A	281.48	0.10	6.68
10Ce/ZSM-5	289.65	0.11	6.83
10Ce-10Fe/ZSM-5	213.97	0.08	10.05
10Ce-10Fe/ZSM-5-A	208.60	0.07	9.90

^a BET surface area. ^b Total pore volume. ^c Average pore diameter.

3.3 Pore analysis

The BJH pore diameter distribution curves of the catalysts are shown in Fig. 4, and the textural properties of the catalysts are listed in Table 3. 0Fe/ZSM-5 possesses mesoporous molecular sieves with a large specific surface area of 341.49 m² g⁻¹. It can be observed from Fig. 5 that the pores in the ZSM-5 carriers are between 2–4 nm, and the apertures distributed in range of 10–100 nm could be secondary pore structures between carriers or active components loaded on the surface of the carriers. After Fe loading, the number of 2–4 nm mesopores slightly declined, and the secondary pores between 10–100 nm relatively increased. Therefore, the specific surface area and pore volume decreased, and the average pore diameter gradually increased. With an increase in Fe content, there was almost no change in the amount of mesopores and secondary pores in 10Fe/ZSM-5, similar with 10Ce/ZSM-5. For 10Ce-10Fe/ZSM-5, the change in number of mesopores was not evident, but the number of secondary pores remarkably increased, leading to a further reduction in specific surface area and pore volume, and the increase in average pore diameter. Combined with the flash catalyst, the mesopores in the used catalyst slightly decreased, and the change in secondary pores was relatively significant, so the average pore diameter of the used catalyst became smaller.

3.4 XPS results

The XPS spectra are shown in Fig. 5, and Table 4 lists the binding energy and calculated relative percentage of ions by

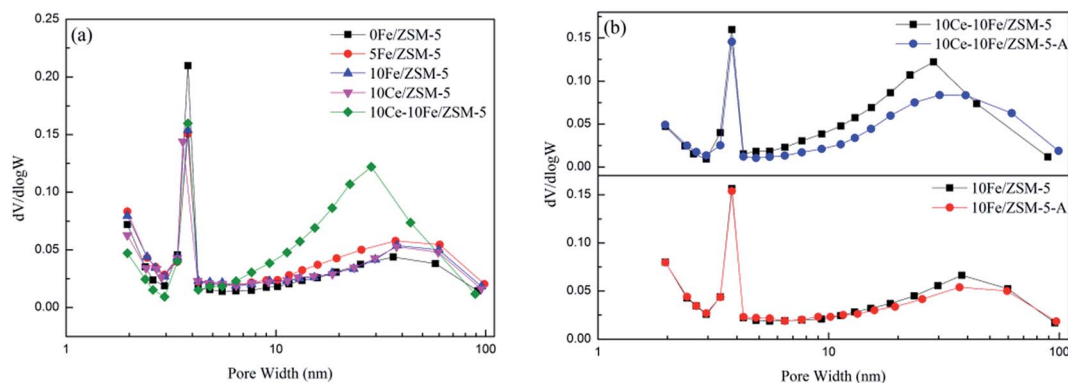


Fig. 4 BJH pore diameter distribution curves of the (a) flash catalysts and (b) used catalysts.



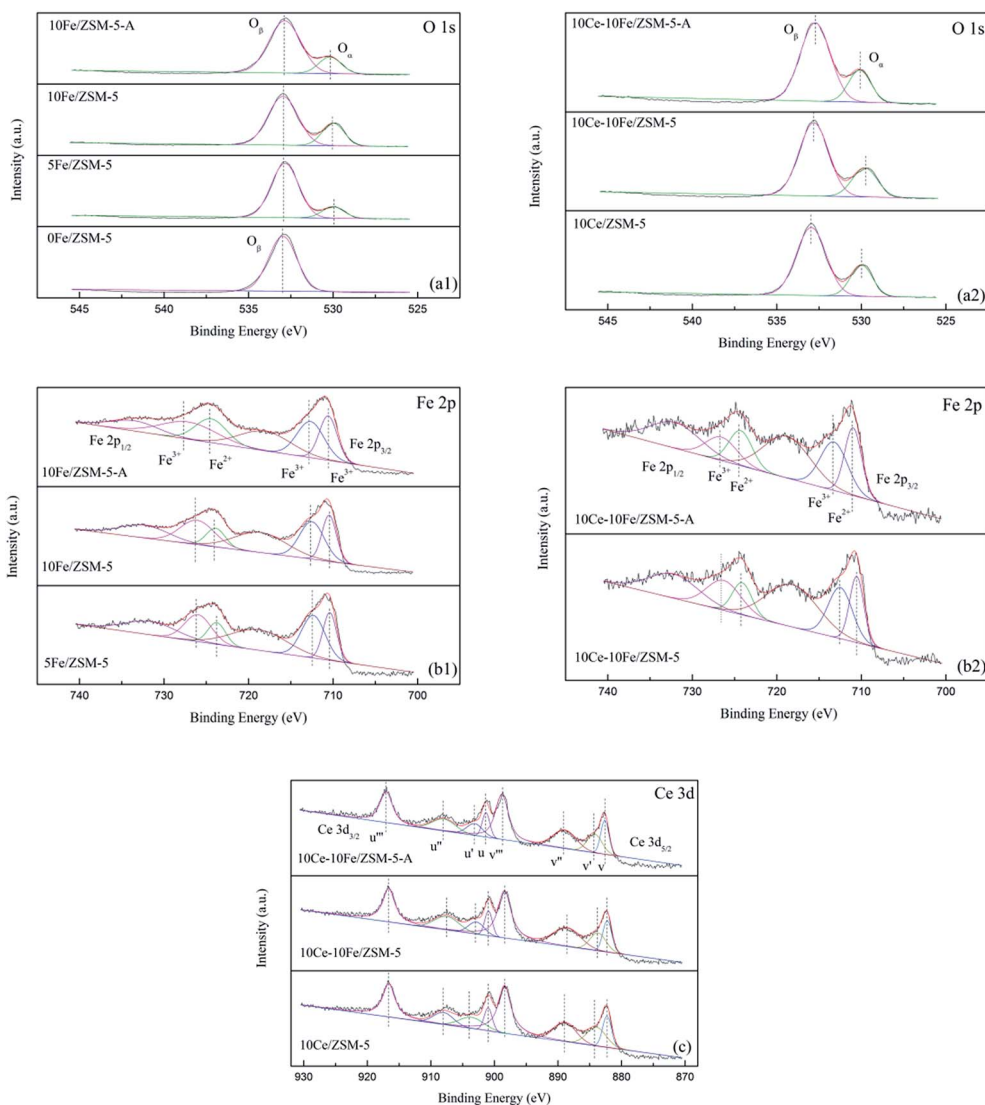


Fig. 5 XPS spectra of (a1 and a2) O 1s, (b1 and b2) Fe 2p, and (c) Ce 3d for the catalysts.

XPS. It can be clearly observed that the O 1s peak is asymmetric and could be deconvoluted into two peaks at 533.0 eV and 530.0 eV, which indicate that different types of oxygen species existed on the catalyst surface. The peak (O_{β}) at 533.0 eV is attributed to chemisorbed oxygen (O_2^- and O^-) and the peak at the binding energy of 530.0 eV (O_{α}) is due to lattice oxygen (O^{2-}). Only chemisorbed oxygen existed in the 0Fe/ZSM-5 catalyst and lattice oxygen appeared after the Fe and Ce loading, which confirms that the oxygen vacancy belonged to the Fe(Ce)-O-Fe(Ce) bond in the catalysts. With an increase in Fe content, the proportion of lattice oxygen increased markedly. Together with the catalytic activity analysis, lattice oxygen in catalysts was presumably helpful in improving their catalytic activity. After loading Ce, there was no evident change in the lattice oxygen content. Various cations such as Fe^{3+} , Fe^{2+} , Ce^{4+} and Ce^{3+} coexisted in the catalysts; thus, the charge mismatching promoted the formation of oxygen vacancies. The Fe 2p_{3/2} peak at about 711 eV could be deconvoluted into two peaks

at 712.3–713.1 eV and 710.4–711.0 eV, which are related to Fe^{3+} and Fe^{2+} , respectively. With an increase in Fe content in the catalyst, the amount of Fe^{3+} slightly reduced and that of Fe^{2+} relatively increased, promoting a redox reaction between Fe^{3+} and Fe^{2+} ($Fe^{2+} + [O] \leftrightarrow Fe^{3+}$). Similarly, the change in Fe^{3+} content was not significant after the Ce loading. Ce in the catalyst was primarily in the form of Ce^{4+} . The Ce 3d_{5/2} peaks were decomposed into four peaks (v''' , v'' , v' and v), where v' at 883.7–884.2 eV belongs to Ce^{3+} , and the others are attributed to Ce^{4+} . Due to the coexistence of Ce^{4+} and Ce^{3+} , Ce^{4+}/Ce^{3+} redox couples exist in the catalysts, which are beneficial for storage and the release oxygen through $Ce^{3+} + [O] \leftrightarrow Ce^{4+}$. The ratio of Ce^{4+} in 10Ce-10Fe/ZSM-5 was lower than that in 10Ce/ZSM-5 because the interaction between Ce and Fe enhanced the redox ability of the catalysts. In addition, the Ce^{4+} content barely changed for 10Ce-10Fe/ZSM-5 after denitration. The Fe^{3+} content decreased by 6–8% from 0.56 to 0.51 because Fe^{3+} was reduced to Fe^{2+} in the reducing atmosphere (CO), which is



Table 4 The binding energy and relative percentage of ions by XPS

Sample	O 1s			Fe 2p _{3/2}			Ce 3d _{5/2}	
	O _β (eV)	O _α (eV)	O _α /(O _α + O _β)	Fe ³⁺ (eV)	Fe ²⁺ (eV)	Fe ³⁺ /(Fe ²⁺ + Fe ³⁺)	Ce ³⁺ (eV)	Ce ⁴⁺ /(Ce ³⁺ + Ce ⁴⁺)
0Fe/ZSM-5	533.0	—	0	—	—	—	—	—
5Fe/ZSM-5	532.9	530.0	0.14	712.3	710.4	0.61	—	—
10Fe/ZSM-5	533.0	530.0	0.26	712.5	710.5	0.58	—	—
10Fe/ZSM-5-A	532.9	530.2	0.18	712.8	710.6	0.54	—	—
10Ce/ZSM-5	532.9	530.0	0.25	—	—	—	883.9	0.88
10Ce-10Fe/ZSM-5	532.8	529.8	0.25	712.5	710.6	0.56	883.7	0.85
10Ce-10Fe/ZSM-5-A	532.7	530.1	0.23	713.1	711.0	0.51	884.2	0.84

consistent with the conclusion from XRD. In addition, the lattice oxygen content in 10Fe/ZSM-5-A was 0.18, which decreased by 30% compared to 0.26 for the flash catalyst, which shows that irreversible changes occurred in the physical and chemical properties of the catalyst during the denitration process. However, the lattice oxygen content in 10Ce-10Fe/ZSM-5-A was reduced by only 8% as a result of the interaction between Fe₂O₃ and CeO₂ ($\text{Ce}^{3+} + \text{Fe}^{3+} \leftrightarrow \text{Ce}^{4+} + \text{Fe}^{2+}$), which implies that the lattice oxygen was effectively restored and the resistance to O₂ and SO₂ improved.

3.5 Results of NH₃-TPD

Fig. 6 shows the NH₃-TPD profiles of the catalysts, in which all the catalysts display three peaks. The peak centered at about 100 °C belongs to NH₃ adsorbed on Lewis acid sites and physically adsorbed on the weak surface acid sites. The peak between 150–300 °C is ascribed to NH₃ adsorbed on the Lewis acid sites, which are medium-strong acid sites. The peak between 300–500 °C is attributed to NH₃ adsorbed on Bronsted acid sites, which are strong surface acid sites. The peak intensity in the profiles represents the total quantity of acid, which slightly changed after Fe loading. After Ce loading, the acid quantity significantly decreased. The temperature and area percent of desorption peaks are shown in Table 5. The percentage of weak acid on the catalyst reduced after the Fe and Ce loading, and the strong acid sites increased. In addition, the total quantity of acid for the used 10Fe/ZSM-5-A and 10Ce-10Fe/

ZSM-5-A catalyst evidently decreased, but the acid quantity of 10Fe/ZSM-5-A was relatively lower than that in the 10Ce-10Fe/ZSM-5-A catalyst, which illustrates that the interaction between Ce and Fe was helpful to remain active. The percentage of strong acid on the 10Fe/ZSM-5-A catalyst sharply decreased compared with that in the flash catalyst. The percentage of strong acid on the 10Ce-10Fe/ZSM-5-A catalyst also declined, but the percentage of medium-strong acid also slightly decreased. It was conjectured that the strong acid sites and some of the medium-strong acid sites were both involved in the catalytic reaction as the active sites for the 10Ce-10Fe/ZSM-5 catalyst. It was also inferred that there was an interaction between Ce and Fe, which is consistent with the XPS analysis.

3.6 Reduction behavior of the catalysts (CO-TPR)

The CO-TPR profiles of the catalysts showed CO consumption in the entire range of temperature used in the analysis. There are three reduction peaks shown in Fig. 7(a). The peak at about 100 °C is related to the reduction of reactive oxygen species (O[−] or O^{2−}). The second peak between 100–500 °C is ascribed to the reduction of Fe³⁺ to Fe²⁺, and the peak above 500 °C is attributed to the reduction from Fe²⁺ to Fe⁰. The CO-TPR profile of the 0Fe/ZSM-5 catalyst without any reduction peaks shows that the 0Fe/ZSM-5 catalyst had no reduction activity. When the Fe content increased from 5% to 10%, the reduction temperature range from 455.4–621.0 °C broadened to 292.5–715.9 °C, indicating that the increase in the active components enhanced the

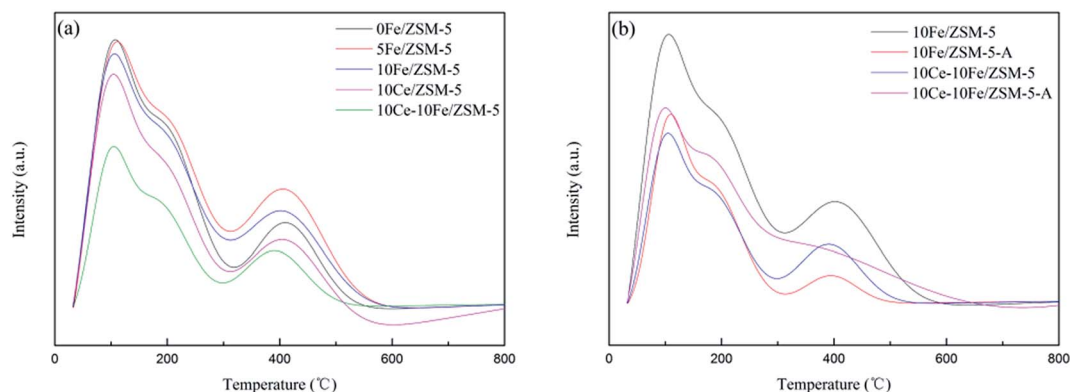


Fig. 6 NH₃-TPD profiles of the (a) flash catalysts and (b) used catalysts.



Table 5 The temperature and area percent of the desorption peaks in NH_3 -TPD

Catalysts	Peak of weak acid		Peak of medium-strong acid		Peak of strong acid	
	$T/^\circ\text{C}$	Area percent/%	$T/^\circ\text{C}$	Area percent/%	$T/^\circ\text{C}$	Area percent/%
0Fe/ZSM-5	99	27.61	186	52.34	410	20.05
5Fe/ZSM-5	101	23.02	189	47.29	406	29.69
10Fe/ZSM-5	97	23.35	183	48.95	402	27.70
10Fe/ZSM-5-A	103	35.0	179	54.62	394	9.48
10Ce/ZSM-5	98	26.14	180	49.32	405	24.54
10Ce-10Fe/ZSM-5	98	27.07	176	49.67	390	23.26
10Ce-10Fe/ZSM-5-A	97	39.43	187	44.28	384	16.29

reducing ability, and promoted the reduction from Fe^{3+} to Fe^{2+} and the formation of oxygen vacancies. This is the reason of decrease in $T_{10\%}$ (Fig. 1). For the 10Fe/ZSM-5-A catalyst used in the catalytic reaction at 650°C , the reduction peak of Fe^{3+} to Fe^{2+} almost completely disappeared. The broad peak for 10Ce/ZSM-5 in Fig. 7(b) at 429.7°C is related to Ce^{4+} to Ce^{3+} . After the Ce loading, the reduction peaks of Fe^{3+} to Fe^{2+} disappeared, indicating that the interaction of Ce and Fe was helpful to restrain the Fe^{3+} reduction, which is consistent with the results of XPS analysis. The peak for Ce^{4+} to Ce^{3+} conversion in 10Ce-10Fe/ZSM-5 shifted to a low temperature as a result of this interaction ($\text{Ce}^{3+} + \text{Fe}^{3+} \leftrightarrow \text{Ce}^{4+} + \text{Fe}^{2+}$). 10Ce-10Fe/ZSM-5-A retained the peaks of the flash catalyst, which suggests that the service life of the catalyst could be improved.

3.7 CO or/and NO interaction with the 10Ce-10Fe/ZSM-5 catalyst

The *in situ* DRIFTS results of CO adsorption on the 10Ce-10Fe/ZSM-5 catalyst are shown in Fig. 8(a). The peak at 1636 cm^{-1} is attributed to bidentate bicarbonate, two peaks at 1551 cm^{-1} and 1473 cm^{-1} belong to the surface carbonate species, and the peak at 1366 cm^{-1} is assigned to bidentate formate.²² Their intensities all decreased with an increase in temperature and disappeared completely at 250°C due to decomposition. Similarly, the peaks 2175 cm^{-1} and 2117 cm^{-1} attributed to M-CO became weaker with the increase in temperature, which disappeared at 300°C due to desorption. The intensity of the peaks

attributed to gaseous CO_2 centered at 2360 cm^{-1} and 2341 cm^{-1} increased as the temperature increased. This indicates that Ce^{4+} or/and Fe^{3+} in a high state were reduced to Ce^{3+} or/and Fe^{2+} under the CO atmosphere, and the released oxygen vacancies oxidized CO to CO_2 .

There were a variety of different NO adsorption species at low temperature (Fig. 8(b)). The peak at 1857 cm^{-1} is attributed to M-NO, which disappeared when the temperature reached 150°C . The peaks for the bridging bidentate nitrates (1602 cm^{-1}), chelated nitrates (1577 cm^{-1}), hyponitrites (1344 cm^{-1}), linear nitrites (1315 cm^{-1}) and chelated nitrites (1284 cm^{-1}) all reduced greatly with the increase in temperature and disappeared completely at 200°C . The similar peaks of the bridging monodentate nitrates (1533 cm^{-1} and 1186 cm^{-1}) disappeared completely at 300°C .¹⁰ The peaks for the bridged nitro at 1544 cm^{-1} and nitrate at 1382 cm^{-1} could be produced in the decomposition process,¹⁹ and their disappearance at high temperature also confirms this assumption. Furthermore, at 250°C , a new peak appeared at 1566 cm^{-1} , which is assigned to chelated nitrates, and its intensity strengthened with the increase in temperature. From the shift in this peak, it was surmised that the NO species adsorbed on the catalyst surface were not only attributed to simple adsorption and decomposition, but the species could have been further restructured.

In situ DRIFTS was performed under simulative reaction conditions, which provides information about the changes in the surface absorbed species in order to investigate the

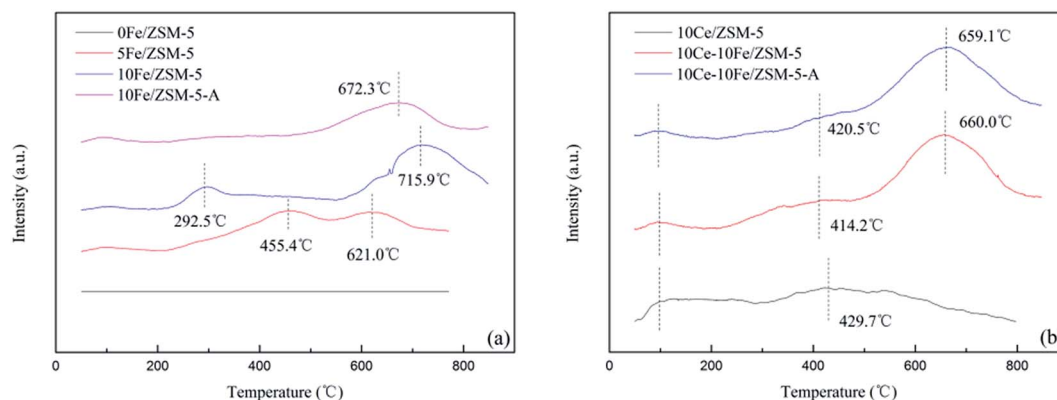


Fig. 7 CO-TPR profiles of the (a) Fe/ZSM-5 catalysts and (b) Ce-Fe/ZSM-5 catalysts.



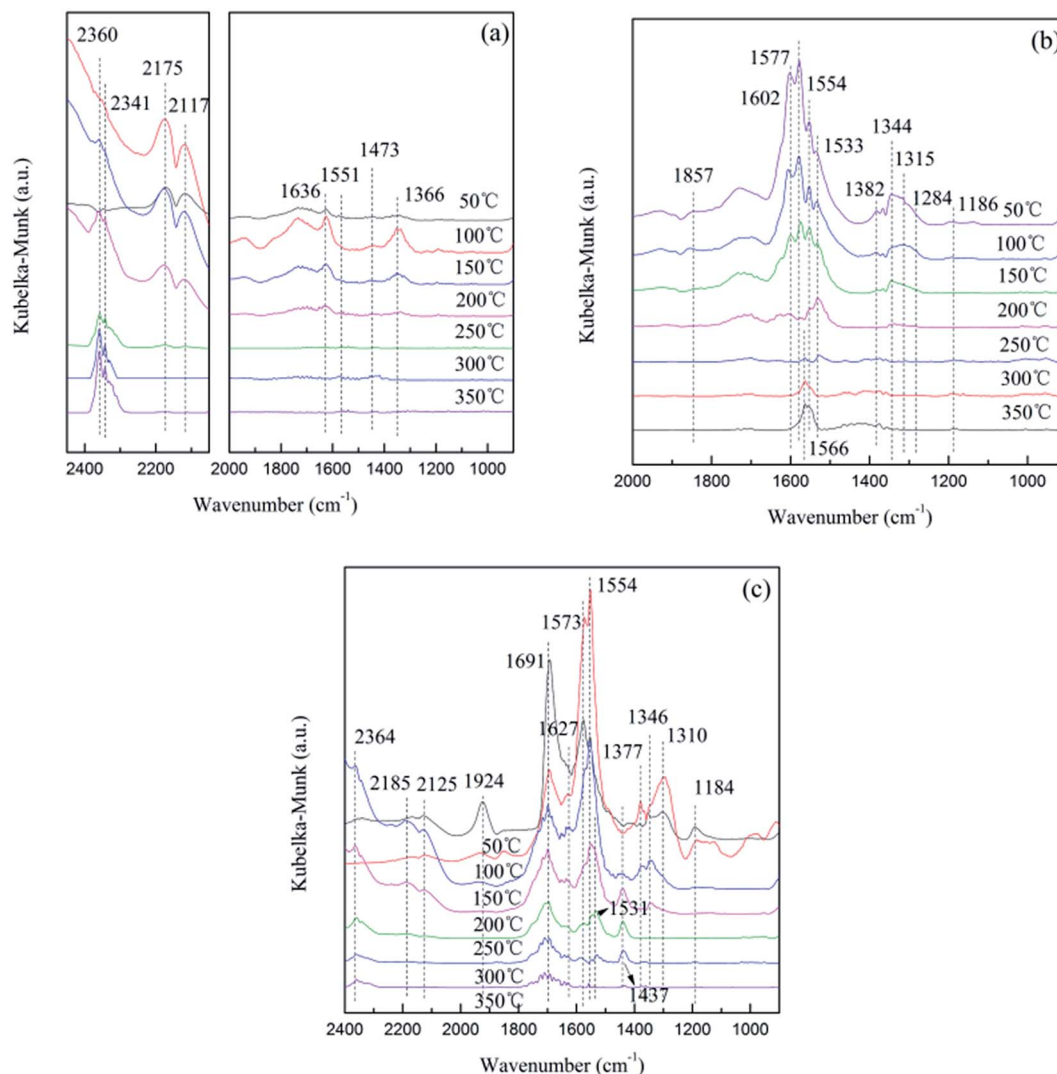


Fig. 8 *In situ* DRIFTS results of (a) CO adsorption, (b) NO adsorption, and (c) CO + NO adsorption on the 10Ce–10Fe/ZSM-5 catalyst from 50–350 °C.

interaction of the reactant gas with the catalyst as shown in Fig. 8(c). At low temperature, the peaks attributed to CO adsorption species were not significant, and the major adsorption states were NO adsorption species. The differences between the spectra in Fig. 8(b) were that: (1) the peak for chelated nitrites was not observed; (2) the peak for the bridging bidentate nitrates (1691 cm^{-1}) increased at $100\text{ }^{\circ}\text{C}$, and did not disappear; (3) the peak intensities of the chelated nitrates (1573 cm^{-1}) and linear nitrites (1310 cm^{-1}) increased at $100\text{ }^{\circ}\text{C}$ then greatly decreased. When the temperature reached $150\text{ }^{\circ}\text{C}$, peaks for CO absorption species appeared gradually, such as gaseous CO_2 (2360 cm^{-1}), M-CO (2185 cm^{-1} and 2125 cm^{-1}), bidentate bicarbonate (1627 cm^{-1}) and carbonate species (1437 cm^{-1} and 1531 cm^{-1}). These peaks first strengthened and then weakened as the temperature increased.

The following conclusions can be deduced through comprehensive analysis: (1) NO was preferentially adsorbed on the catalyst surface due to unpaired electrons, $\text{NO}_{(\text{g})} \rightarrow \text{NO}_{(\text{ads})}$;

(2) the NO absorption species gradually decomposed with an increase in temperature, and CO adsorbed on the released active sites, $\text{CO}_{(\text{g})} \rightarrow \text{CO}_{(\text{ads})}$; and (3) Ce^{4+} or/and Fe^{3+} in a high state were reduced to Ce^{3+} or/and Fe^{2+} by CO, and the released oxygen vacancies were advantageous for the activation of N–O and promoted the decomposition of NO, $\text{NO}_{(\text{ads})} \rightarrow \text{N}_{(\text{ads})} + \text{O}_{(\text{ads})}$. Then, the adsorption species on the catalyst surface were restructured, $\text{CO}_{(\text{ads})} + \text{O}_{(\text{ads})} \rightarrow \text{CO}_{2(\text{ads})}$, $\text{NO}_{(\text{ads})} + \text{N}_{(\text{ads})} \rightarrow \text{N}_2\text{O}_{(\text{ads})}$, $\text{N}_{(\text{ads})} + \text{N}_{(\text{ads})} \rightarrow \text{N}_{2(\text{ads})}$ and $\text{O}_{(\text{ads})} + \text{O}_{(\text{ads})} \rightarrow \text{O}_{2(\text{ads})}$. Finally, the products (CO_2 , N_2O , N_2 and O_2) were obtained after desorption, $\text{CO}_{2(\text{ads})} \rightarrow \text{CO}_{2(\text{g})}$, $\text{N}_2\text{O}_{(\text{ads})} \rightarrow \text{N}_2\text{O}_{(\text{g})}$, $\text{N}_{2(\text{ads})} \rightarrow \text{N}_{2(\text{g})}$, $\text{O}_{2(\text{ads})} \rightarrow \text{O}_{2(\text{g})}$.

4. Conclusions

The Ce–Fe/ZSM-5 catalysts prepared *via* an impregnation method showed better catalytic performances than Fe/ZSM-5 for NO removal by CO in the presence of O_2 , SO_2 and steam.



The 10Ce–10Fe/ZSM-5 catalyst exhibited stable NO conversion of over 90% within the temperature range from 320 °C to 650 °C, and it had superior resistance to O₂, SO₂ and steam. As the contents of Fe and Ce increased, the ZSM-5 structure was still retained, diffraction peaks of Fe₂O₃ and CeO₂ were observed *via* XRD, the specific surface area and pore volume decreased, and the average pore diameter increased. From the XPS results, the Ce–Fe/ZSM-5 catalysts possessed chemisorbed oxygen and lattice oxygen, and various cations (Fe³⁺/Fe²⁺ and Ce⁴⁺/Ce³⁺) promoted the production of oxygen vacancies, which were advantageous for the activation of N–O and in agreement with the CO-TPR results. Not only strong acid sites, but also some medium-strong acid sites were involved in the catalytic reaction as the active sites for the 10Ce–10Fe/ZSM-5 catalyst in NH₃-TPD. The interaction between Fe₂O₃ and CeO₂ (Ce³⁺ + Fe³⁺ ↔ Ce⁴⁺ + Fe²⁺) in the 10Ce–10Fe/ZSM-5 catalyst, which was confirmed by XPS, NH₃-TPD and CO-TPR, improved the catalytic performance, reducing property, resistance to O₂, SO₂ and steam, and the service life of the catalyst.

Conflicts of interest

There are no conflicts to declare.

Acknowledgements

Financial support of this work was provided by the National Natural Science Foundation of China (No. 51274060).

References

- 1 C. Xu, J. Liu, Z. Zhao, F. Yu, K. Cheng, Y. Wei, A. Duan and G. Jiang, *J. Environ. Sci.*, 2015, **31**, 74.
- 2 K. Zhao, W. Han, G. Lu, J. Lu, Z. Tang and X. Zhen, *Appl. Surf. Sci.*, 2016, **379**, 316.
- 3 M. Shen, C. Li, J. Wang, L. Xu, W. Wang and J. Wang, *RSC Adv.*, 2015, **5**, 35155.
- 4 B. Dou, G. Lv, C. Wang, Q. Hao and K. Hui, *Chem. Eng. J.*, 2015, **270**, 549.
- 5 W. Shan, F. Liu, H. He, X. Shi and C. Zhang, *Appl. Catal., B*, 2012, **115–116**, 100.
- 6 R. Zhang, Q. Zhong, W. Zhao, L. Yu and H. Qu, *Appl. Surf. Sci.*, 2014, **289**, 237.
- 7 J. Wang, Z. Yan, L. Liu, Y. Zhang, Z. Zhang and X. Wang, *Appl. Surf. Sci.*, 2014, **309**, 1.
- 8 X. Lou, P. Liu, J. Li, Z. Li and K. He, *Appl. Surf. Sci.*, 2014, **307**, 382.
- 9 X. Yao, F. Gao, Y. Cao, C. Tang, Y. Deng, L. Dong and Y. Chen, *Phys. Chem. Chem. Phys.*, 2013, **15**, 14945.
- 10 X. Yao, Y. Xiong, J. Sun, F. Gao, Y. Deng, C. Tang and L. Dong, *J. Rare Earths*, 2014, **32**, 131.
- 11 Y. Lv, L. Liu, H. Zhang, X. Yao, F. Gao, K. Yao and L. Dong, *J. Colloid Interface Sci.*, 2013, **390**, 158.
- 12 N. Liu, X. Chen, J. Zhang and J. Schwank, *Catal. Today*, 2015, **258**, 139.
- 13 L. Liu, Q. Yu, J. Zhu, H. Wan, K. Sun, B. Liu, H. Zhu, F. Gao, L. Dong and Y. Chen, *J. Colloid Interface Sci.*, 2010, **349**, 246.
- 14 X. Yao, F. Gao, Q. Yu, L. Qi, C. Tang, L. Dong and Y. Chen, *Catal. Sci. Technol.*, 2013, **3**, 1355.
- 15 C. A. Sierra-Pereira and E. A. Urquieta-González, *Fuel*, 2014, **118**, 137.
- 16 J. Li, S. Wang, L. Zhou, G. Luo and F. We, *Chem. Eng. J.*, 2014, **255**, 126.
- 17 S. M. Alipour, *Chin. J. Catal.*, 2016, **37**, 671.
- 18 M. Moreno-Recio, J. Santamaria-González and P. Maireles-Torres, *Chem. Eng. J.*, 2016, **303**, 22.
- 19 L. Zhu, L. Zhang, H. Qu and Q. Zhong, *J. Mol. Catal. A: Chem.*, 2015, **409**, 207.
- 20 B. Li, Z. Huang, X. Huang, S. Kou, F. Liu, X. Zhang and H. Yang, *RSC Adv.*, 2016, **6**, 6300.
- 21 X. Cheng, X. Zhang, M. Zhang, P. Sun, Z. Wang and C. Ma, *Chem. Eng. J.*, 2017, **307**, 24.
- 22 C. Deng, B. Li, L. Dong, F. Zhang, M. Fn, G. Jin, J. Gao, L. Gao, F. Zhang and X. Zhou, *Phys. Chem. Chem. Phys.*, 2015, **17**, 16092.
- 23 K. Liu, F. Liu, L. Xie, W. Shan and H. He, *Catal. Sci. Technol.*, 2015, **5**, 2290.
- 24 S. Lai, D. Meng, W. Zhan, Y. Guo, Y. Guo, Z. Zhang and G. Lu, *RSC Adv.*, 2015, **5**, 90235.
- 25 G. Carja, Y. Kameshima, K. Okada and C. D. Madhusoodana, *Appl. Catal., B*, 2007, **73**, 60.

